Intrinsic Variability of Lithium Metal Foils and Its Impact on Rechargeable Battery Performance

Kun Wang
University of Chicago
Sravani Duggirala
University of Chicago
Vincent Ji
University of Chicago
Bhargav Bhamwala
University of California, San Diego
Kun Ryu
University of Chicago
Mingqian Li
University of California, San Diego
Shen Wang
University of California, San Diego
Kathryn Hicks
University of Chicago
Wurigumula Bao
University of Chicago
Ying Shirley Meng
shirleymeng@uchicago.edu
University of Chicago

Research Article

Keywords:

Posted Date: May 12th, 2026

DOI: https://doi.org/10.21203/rs.3.rs-8875953/v1

Additional Declarations: No competing interests reported.

Abstract

Lithium metal anodes (LMAs) offer unrivaled theoretical capacity and the lowest electrochemical potential among practical anode materials, making them central to high energy density battery chemistries. Yet in most studies, the lithium foil itself is treated as a nominally interchangeable component, and the impact of its intrinsic variability on cell behavior remains poorly quantified. Here we systematically investigate how initial-state properties of commercial lithium foils influence electrochemical performance. Using a diverse sample set of 17 foils spanning manufacturing routes, thicknesses, and storage histories, we quantify key bulk, surface, and microstructure descriptors. By utilizing a combination of electrochemical measurements, surface optical and wetting characterization, and structural and chemical analyses, we correlate initial state descriptors to plating/stripping behavior, rate capability, and capacity retention. These descriptors are then correlated with plating/stripping behavior in Li||Cu cells and with rate capability and capacity retention in Li||NMC622 full cells. Our results reveal that lithium inventory, surface passivation state, and microstructure each play distinct and complementary roles in governing cell performance. True lithium inventory primarily dictates the onset of lithium depletion. Optical lightness and electrolyte contact angle, which reflects the degree of surface passivation, correlates with the overpotential in electrochemical process; microstructural features such as grain size and texture influence stripping/plating homogeneity and the evolution of interfacial morphology. On this basis, we propose a practical workflow and set of screening criteria for lithium-foil quality assessment prior to cell assembly, combining simple, experimentally accessible metrics with targeted structural and chemical analysis when needed. The framework provides mechanistic insight into how variability in commercial lithium foils translates into cell-level behavior and offers actionable guidance for material selection, processing, and storage in lithium-metal battery development.

Introduction

Rechargeable lithium-ion batteries (LIBs) have achieved remarkable commercial success and now underpin most portable electronics, electric vehicles, and grid-scale storage systems.[1] However, further increasing gravimetric energy density with conventional graphite anodes is fundamentally constrained.[2] State-of-the-art LIBs employing graphite anodes can deliver 250–300 Wh/kg and are already approaching their theoretical energy-density limit, despite incremental improvements in recent years.[3, 4] Lithium metal batteries (LMBs) are widely recognized as one of the most promising candidates to overcome this limitation.[5] Lithium metal anodes (LMA) offer unprecedented electrochemical performance with a high theoretical capacity of 3860 mAh/g and the lowest electrochemical potential (–3.04 V versus the standard hydrogen electrode) among all practical anode candidates.[6] Their low density of only 0.534 g/cm³ further contributes to gravimetric advantages, enabling significant weight reduction compared with graphite-based systems. The specific energy density of cells utilizing LMAs has been reported to surpass 500 Wh/kg,[7, 8] highlighting the critical role of lithium metal as a cornerstone material for next-generation energy storage systems requiring high gravimetric energy density.

Despite more than six decades of research on LMAs, practical deployment has been hindered by severe safety and reliability challenges.[9] Considerable efforts have been devoted to electrolyte engineering,[10] cathode optimization,[11] and anode architecture/protection[12] to enable stable cycling of lithium metal. While these approaches have led to important progress, they largely treat the lithium metal itself as a passive, interchangeable component whose intrinsic properties are assumed to be uniform across sources and grades.[13]

Recent studies have begun to challenge this assumption by showing that the intrinsic quality of lithium metal can strongly influence electrochemical performance. Existing studies have reported that pristine commercial LMAs exhibit highly scattered bulk and surfaces composition,[14–20] reflecting strong supplier and storage dependence. Variations in bulk purity and trace impurity content have been correlated with differences in SEI composition and cycling stability.[21] Surface chemistry and morphology, shaped by manufacturing, storage environment, and handling, can alter wetting behavior, nucleation overpotential, and local current distribution during plating and stripping.[22–28] At the same time, the microstructure of lithium metal—grain size, crystallographic texture, dislocation density, and defect populations—has been shown to affect mechanical response, mass transport, and localized deformation under electrochemical cycling.[20, 29–32] The primary crystal orientation of commercial lithium foils, however, varies considerably due to differences in fabrication parameters and post-fabrication processes with mean grain sizes spanning from submicron to over 250 μm.[14, 16, 29, 30, 33] Together, these studies suggest that the initial state of commercial lithium foils is an important, yet insufficiently controlled, factor that can modulate LMA performance even under nominally identical cell designs.

Nevertheless, existing reports examine only a small number of samples, which limits statistical confidence and makes it difficult to determine whether observed trends are generic or vendor specific. In addition, characterization methods and cycling protocols vary widely between studies, including differences in electrolyte formulation, current density, cutoff criteria, and cell geometry, complicating any attempt to separate intrinsic material effects from testing artifacts. More importantly, prior works usually focus on a single descriptor, such as impurity concentration,[21] surface chemistry,[14] or grain structure,[20] rather than treating lithium reservoir, bulk composition, surface chemistry, and microstructure as a coupled set of variables that jointly govern lithium plating and stripping. In practical settings, lithium foils are sourced from different vendors, produced via distinct casting and rolling routes, supplied in various thicknesses and formats, and subjected to different storage and handling histories. Yet there is currently no standardized framework to evaluate their quality prior to cell assembly, nor clear guidance on which measurable properties most strongly predict electrochemical performance. Consequently, the field still lacks a unified, mechanistic understanding of how lithium-foil variability translates into cell-level behavior.

This work addresses this critical gap by systematically investigating how intrinsic variability among commercial lithium foils influences their electrochemical behavior. We examine 17 lithium foils that span a wide range of manufacturing origins, thicknesses, and storage histories. For each foil, we quantify key bulk, surface, and microstructural descriptors, including impurity content, surface chemistry and optical appearance, and grain structure, using a combination of elemental analysis and advanced characterization techniques. These metrics are then correlated with plating/stripping behavior in Li||Cu coin cells and Li||NMC622 coin, enabling a direct mapping between initial-state descriptors and cell-level electrochemical response. By integrating these datasets, we identify a set of experimentally accessible parameters that most strongly govern LMA performance and propose a practical framework for lithium-foil quality assessment. The resulting guidelines are intended to support more rational material selection, processing, and handling practices, and to facilitate reproducible research and development toward reliable, high energy density LMBs.

Results

Integrated characterization workflow for assessing variability in lithium metal foils

To analyze how intrinsic variability in commercial lithium foils arises and impacts electrochemical behavior, we first established an integrated characterization workflow that quantifies their bulk, surface, and microstructural properties, as shown in Fig. 1. Bulk and surface morphology, as well as grain structure, were examined by plasma focused ion beam–scanning electron microscopy (PFIB-SEM) with energy-dispersive X-ray spectroscopy (EDX) and electron backscatter diffraction (EBSD) to reveal the microstructures arising from different manufacturing routes. The metallic lithium inventory was quantified by titration gas chromatography (TGC), providing a direct measure of active Li^0. Total lithium and trace-metal impurities introduced during the manufacturing process were determined by inductively coupled plasma mass spectrometry (ICP-MS). Together, TGC and ICP-MS allow us to distinguish metallic lithium from nonmetallic lithium-containing species and to estimate the metallic-lithium fraction. Surface passivation and interphase composition were probed by X-ray photoelectron spectroscopy (XPS) to identify key inorganic and organic species that regulate interfacial reactivity. In addition, colorimetry and electrolyte-wetting measurements were introduced as straightforward yet effective descriptors of interphase stability and cycling performance. Colorimetry provides a rapid visual indicator of surface oxidation and uniformity. Wetting tests, in contrast, probe the dynamic spreading of electrolyte on passivated lithium surfaces. By integrating these measurements, the workflow generates a multidimensional descriptor set that links lithium metal quality, interphase behavior, and electrochemical performance.

A total of 17 lithium foils were received in diverse forms and conditions, as summarized in Table 1. We examined foils across a broad thickness range, including conventional thick foils (100 μm), thin foils (20–50 μm), and ultrathin foils (≤ 20 μm), to assess how lithium inventory and thickness influence material quality and electrochemical behavior. All thin (20–50 μm) and thick (≥ 100 μm) lithium foils in this study were produced by conventional extrusion and rolling methods, which generally cannot achieve thicknesses below ~ 20 μm due to mechanical limitations.[7] In contrast, the ultrathin foils (≤ 20 μm) include both rolled (20 μm) and vapor-deposited samples, as physical vapor deposition (PVD) techniques such as thermal evaporation enable sub-20 μm lithium fabrication. Fourteen foils were supplied as lithium on a copper substrate, leveraging the Cu support for mechanical robustness and handling stability, while three foils with thicknesses of 40 μm or greater were received as freestanding lithium. The lithium samples arrived in distinct packaging conditions with different gas fills, transportation histories, storage environments, and calendar ages, all of which introduce additional variability beyond fabrication differences. It is also worth noting that the foils in this study were not all sourced directly from original manufacturers; a portion was obtained through distributors or secondary suppliers, further reflecting the diversity of procurement channels encountered in practice. In this work, we treat the ensemble of foils as a practical snapshot of the commercial landscape and focus on relating the initial state of each as-received sample to its electrochemical performance, rather than on ranking or benchmarking fabrication quality across vendors. A more detailed analysis of the effects of specific production routes, handling conditions, and storage duration is beyond the scope of this work and will be addressed in a separate study.

Table 1
Summary of examined lithium metal foil samples obtained from commercial suppliers.

Quantifying True Lithium Inventory as a Key Descriptor of Foil Quality

Building on the integrated characterization workflow above, we first quantify the true metallic lithium inventory in each commercial foil. In practical cells, the amount of electrochemically active Li^0 directly sets the negative-to-positive (N/P) capacity ratio, which governs both the onset of lithium depletion during cycling and the energy density of the battery. Therefore, accurately determining the thickness of active Li^0, rather than relying solely on nominal specifications, is essential for interpreting electrochemical behavior. PFIB-SEM cross-sections reveal the overall layer structure of the lithium foils, including the metallic lithium, copper current collector, and any interfacial defects (Fig. 2a–2g; full PFIB-SEM images in Figures **S1–S3**). Across all samples, the PFIB-SEM-measured geometric thicknesses cluster closely around the labeled values, with a standard deviation of 1.7 μm (Fig. 2h). Although the overall morphology is relatively uniform across the examined vendors, subtle variations in thickness are still apparent. The 5 μm and 10 μm vapor deposited foils display tightly confined thickness ranges, whereas the thicker foils show slightly larger deviations. A few samples deviate more noticeably, with the maximum discrepancy reaching about 4.2 μm thinner than specified (~ 10.5% of the nominal thickness), likely originating from the mechanical rolling process.

However, PFIB-SEM only provides local thickness information over a limited field of view and cannot easily distinguish native surface layers from metallic lithium across an entire roll or sheet. To obtain a bulk-averaged measure of the metallic lithium inventory, we therefore use TGC to quantify Li^0 thickness for each foil (Fig. 2i). Although the nominal thickness generally captures the physical dimensions of the foil stack (metallic lithium plus surface layers), it does not necessarily reflect the amount of electrochemically available Li^0. Across the 17 foils examined, nearly all contain less active lithium than their labeled thickness would suggest, in some cases by as much as an equivalent thickness of 4.7 μm (0.97 mAh/cm^2). This indicates that the impurities and native surface layers occupy a non-negligible fraction of the total thickness. This behavior is observed for both freestanding and Cu-substrated foils, demonstrating that apparent thickness alone is an incomplete descriptor of the initial lithium reservoir. These findings underscore the importance of directly quantifying Li^0 content when defining N/P ratios and comparing cycling data across foils. In the following analysis of plating/stripping behavior, we therefore treat the true lithium inventory as a key descriptor that sets the baseline lithium inventory.

Optical and Wetting Signatures as Metrics of Lithium Surface Quality

Knowing that the equivalent metallic lithium thickness is consistently lower than the nominal value, a substantial portion of the variability in electrochemical behavior must arise from differences in surface state. In practice, these changes manifest as visible differences in color and lightness,[34, 35] with some foils appearing bright silver-

gray, whereas others exhibit yellow, brown, or darkened tones after storage and handling. To capture these variations in a quantitative manner, we use colorimetry as an optical descriptor of lithium surface quality (Fig. 3a). The colorimeter reports the CIE L*a*b* coordinates for each foil, where a* and b* encode the hue–chroma space (red–green and yellow–blue components), and L* quantifies lightness. A fresh lithium surface exhibits near-zero chromaticity (a* = 0.54, b* = −0.13). Here, “fresh lithium” refers to a reference surface obtained by slicing a flat cross-section from a lithium ingot inside an inert-atmosphere glovebox, which provides a clean, minimally reacted benchmark for comparison. In contrast, most commercial samples cluster in regions of positive a* (from 0 to 25) and positive b* (from 0 to 25), indicating a shift toward red and yellow tones (Fig. 3b). Samples exhibiting higher chroma, meaning more saturated coloration, show elevated stripping overpotentials measured in Li||Cu asymmetric cells. In this configuration, the overpotential is largely governed by Li^+ transport and charge transfer across the native surface layer and any additional SEI, so higher overpotential corresponds to higher interfacial resistance.[36, 37] Therefore, the stripping overpotential serves as a compact descriptor of LMA kinetics and as a key performance metric for comparing commercial foils (**Figure S4**). These observations indicate that intensified color shifts are not merely cosmetic but are closely linked to electrochemical behavior and that stronger chromatic signatures imply a deviation from the fresh lithium surface and the presence of chemically more complex and electrochemically resistive passivation layers that impede uniform stripping.

Among the CIE parameters, the most sensitive and practically useful optical quantity is the lightness L*. Aged or heavily exposed lithium naturally transitions from bright silver-gray to darker colors as surface oxidation products accumulate. In this study, L* offers a direct metric for comparing commercial foils. Values approaching those of fresh lithium (L* = 99.8%) indicate minimal surface alteration, whereas lower L* values correspond to more extensive passivation. Photographic comparisons illustrate these trends, with some foils exhibiting visibly yellow or darkened tones while others retain a more neutral, shiny silver-gray appearance indicative of higher lightness (Fig. 3c). Higher-lightness foils generally exhibit lower interfacial resistance (Fig. 3d). For example, the foil with L* = 99.6% shows the lowest stripping overpotential of 136.0 mV, whereas the foil with L* = 71.4% exhibits the highest overpotential of 471.8 mV in Li||Cu cells. Thickness also plays a role. Samples thicker than 40 μm generally maintain high lightness (> 90%), while ultrathin foils (≤ 20 μm) show much broader variability (95.9%–67.4%). This behavior indicates that improved quality control and storage management are especially critical for thin-Li manufacturing. Notably, the two foils with the lowest lightness (< 75%; foil-1 and foil-4) already exhibited visibly corroded surfaces upon receipt, indicative of significant exposure to moisture and oxygen during shipping and storage (**Figures S5 and S6**). In contrast, the highest lightness values were observed for a foil with a specified polymer coating (foil-13) and another foil with a detectable organic surface coating layer (foil-9). These surface coatings likely acted as barriers that blocked moisture and oxygen during shipping and storage, thereby preventing surface degradation of lithium. To further validate that the overpotential differences reflect interfacial resistance rather than ohmic or mass transport contributions, EIS measurements in Li||Li symmetric cells. Both Rsei and Rct increase with decreasing surface lightness, with the charge transfer resistance showing a more pronounced dependence and dominating the total interfacial resistance in low lightness samples (**Figure S7**). These observations highlight that coating, packaging, shipping, and storage conditions are key determinants of the surface quality of commercial lithium metal. Spearman correlation analysis across all 17 foils confirms these trends quantitatively: lightness L shows the strongest correlation with stripping overpotential ($\rho = -0.631$, $p < 0.01$), followed by color neutrality $-\sqrt{(a^2+b^2)}$ ($\rho = -0.667$, $p < 0.01$) and electrolyte contact angle ($\rho = -0.542$, $p < 0.05$), as summarized in **Table S2**.

Electrolyte wettability offers a complementary indicator of surface condition. Contact-angle on lithium foil surface was measured using a localized high-concentration electrolyte (LHCE, 1.54 M LiFSI in DME:TTE = 22/78 v/v%) (Fig. 3e).[38] Foils exhibiting smaller contact angles (< 15°) also show low lightness (L* < 80%) and tend to deliver high stripping overpotential. This inverse correlation arises because the electrolyte wets the passivation layer more readily than bare metallic lithium. Oxidation products such as Li_2O, LiOH, and Li_2CO_3 introduce polar surface sites and give rise to a built-in dipole layer across the Li metal and surface product interface.[39, 40] At the same time, these surface layers often adopt a rough and porous morphology. This morphology originates from large molar volume differences among the reaction products and from intrinsic stress generated during the formation of the oxide and hydroxide layers.[20, 41] The mechanical fragility of such inhomogeneous surface films promotes microcracking and the formation of pulverized oxidation products (**Figures S5 and S6**), which further increase surface roughness and porosity. Profilometry measurements across all 17 foils reveal surface roughness (Sa) values ranging from 0.24 to 1.21 μm (**Figure S8**). Importantly, the origins of this roughness differ markedly across samples: in heavily oxidized foils, elevated Sa arises from the accumulation of oxidation products visible in SEM-EDX mapping, whereas in others it originates from the native surface texture introduced during manufacturing or from rolling marks. Together, enhanced polarity and textured morphology increase the affinity of the surface for the ether based LHCE and lower the apparent contact angle, yet they simultaneously thicken the transport path for Li^+. As a result, strongly wetting surfaces in this study typically correspond to resistive interphases rather than to more benign lithium interfaces, and they are associated with higher stripping overpotentials. In contrast, foils with moderate contact angles tend to have more compact passivation layers that maintain good ionic transport. Together, the combined use of colorimetry and wettability measurements offers an efficient, low-cost, and scalable methodology for assessing lithium surface quality. The negative correlation between surface descriptors and stripping overpotential is further confirmed using a carbonate electrolyte on a representative subset of foils, demonstrating the generalizability of the screening framework across electrolyte systems (**Figure S11**). These optical and wetting signatures are complementary and provide rapid, non-destructive metrics for screening lithium surface quality prior to cell assembly and motivate more detailed chemical analysis of the passivation layers, as discussed in the following section.

Surface Chemical Composition and Chemical Heterogeneity

The optical and wetting analyses described above reveal substantial heterogeneity among commercial lithium metal surfaces and highlight their strong influence on electrochemical performance. To identify the chemical origins of this variability, we further examined lithium purity alongside detailed surface morphology and composition using ICP-MS, XPS and SEM-EDX. Industrial lithium metal is typically produced via molten salt electrolysis[21] and exhibits purity above 99.5% as produced, with residual Na, Fe, and Mg impurities originating from the precursor brine.[19] **Table S1** shows the levels of these residual impurities in the commercial foils as measured by ICP-MS. Lithium foils prepared by extrusion and rolling contain Na and Mg at levels from several tens of ppm up to more than one hundred ppm, along with Fe at a few ppm. In contrast, the physically vapor-deposited (PVD) lithium foils exhibit much lower impurity levels, with Na below 1 ppm, and Mg and Fe below 0.01 ppm. During PVD, most less-volatile impurities such as Na, Fe, and Mg remain in the crucible due to their very different vapor pressures compared with lithium, which provides a purification effect. Within the impurity levels probed here, however, variations in Na, Mg, and Fe within the range studied do not show a strong direct

correlation with stripping overpotential or cycle life. This indicates that, as-produced bulk metallic impurities are not sufficient on their own to explain the variability in electrochemical performance.

Beyond the as-produced impurities, further changes in bulk and surface composition can occur during foil fabrication as well as subsequent transportation and storage. Metallic lithium is highly reactive toward CO_2, H_2O, O_2, and even N_2,[24] which are ubiquitous in air and can be present at low levels even under practically inert conditions such as dry rooms and gloveboxes. As a result, conventional lithium foils inherently possess a native passivation layer that includes LiOH, Li_2CO_3, and Li_2O on their surfaces. Here we examine lithium purity by combining TGC and ICP-MS, defining metallic lithium purity as the fraction of Li^0 relative to the total lithium content, including surface reaction products and other Li^+ compounds. As shown in Fig. 4a, the metallic lithium purity across all commercial samples ranges from 98.5% down to 83.8%. The lowest purity values appear in ultrathin foils, where the reduced lithium inventory causes surface-derived Li^+ species to represent a more noticeable fraction of the total lithium content. Reduced metallic lithium purity strongly correlates with elevated stripping overpotential, which demonstrates that interfacial resistance increases as oxidation products accumulate (Fig. 4b). Most foils follow this trend, with lower metallic lithium purity associated with higher overpotentials. Within this general behavior, two foils with coated surfaces show particularly low stripping overpotentials among the ultrathin and thin foils despite only modest metallic lithium purity. In these cases, the coating layers may contain lithium in nonmetallic form or may have reacted with metallic lithium to form a layer that facilitates charge transfer. These results indicate that a decrease in metallic lithium purity can arise from either uncontrolled oxidation, which is detrimental, or intentionally engineered surface layers, which can lower the measured purity while still improving interfacial stability and electrochemical performance.

To further elucidate the chemical origins of these purity differences, Fig. 4c contrasts a foil exhibited without protective coating (foil-15) and a sample with protective coating (foil-9). XPS depth profiling of foil-15 reveals a characteristic layered structure comprising an outer region enriched in LiOH, and Li_2CO_3 and an inner region with a higher ratio of Li_2O, consistent with previous reports of lithium metal surface.[22] Besides, a characteristic sharp peak at 52.5 eV is shown in foil-15 that corresponds to metallic lithium. In comparison, the coated foil-9 shows no metallic Li peak in Li 1S XPS spectrum and organic C-O peak at 535.5 eV in O 1S spectrum indicates a homogenous surface coating layer. Broader trends across all samples (**Figures S9-S10**) confirm that foils with lower lightness, lower purity, and higher overpotential consistently show heterogeneous surface components distribution and elevated oxidation content. Two foils that received with visible oxidation on the surface (foil-1 and foil-4) show heterogeneous oxygen-rich domains and irregular surface morphology, while the high-purity foil displays relatively uniform elemental distribution and minimal oxidation features (**Figures S5-S6)**. These findings clarify that maintaining high metallic lithium purity and suppressing heterogeneous oxidation formation are central to achieving a preferable lithium surface. This mechanistic linkage offers guidance for material qualification and process design, highlighting the need for manufacturing routes that minimize atmosphere exposure, handling practices that limit uncontrolled surface reactions, and packaging and coating strategies that preserve a uniform, lightly passivated surface. To further validate the XPS findings and address potential sputtering artifacts, TOF-SIMS depth profiling was performed on representative foils (**Figure S12**). For foil-9, TOF-SIMS confirms the presence of a distinct organic-rich surface layer confined to the outermost ~ 20 nm, beneath which metallic lithium is rapidly recovered, corroborating the XPS interpretation of an intact organic coating. For foil-15, the gradual rise of Li^-, $Li_2CO_3^-$, and LiO^- signals over the probed depth range consistent with the apparent weakening of the Li^0 XPS peak observed during Ar^+ etching of this foil.

Cycling performance variation in LMAs

Ultrathin lithium metal anodes are central to the promise of high-energy rechargeable batteries because they allow aggressive N/P ratios and cell-level energy densities that are unattainable with conventional thick foils.[42–44] From the above discussion, it can be found that for identical nominal thicknesses, lithium foils can exhibit markedly different electrochemical performance depending on their initial states. Figures 5a-5c show the capacity retention of Li||NMC622 cells with ultrathin, thin, and thick lithium foils, respectively. This divergence becomes increasingly pronounced at lower thickness. Ultrathin lithium with 15–20 μm thickness display a much broader foil-to-foil spread in cycle life compared with 40 μm or 100 μm foils. This broader dispersion can be better understood by examining how cycle life scales with the initial metallic lithium thickness, which reveals the sensitivity of thin foils to variations in lithium inventory. Cells with a small lithium inventory of 20 μm exhibit earlier capacity fade, as the active lithium reservoir is exhausted before the end of life, leaving behind porous and electrically isolated regions within the anode (Fig. 5d). In comparison, post-mortem analysis reveals that cells using foil of 40 μm thickness still retain a significant amount of metallic lithium at the end of life, indicating that lithium depletion is no longer the primary failure mode. In these cases, performance degradation is dominated by cumulative interphase growth and voltage polarization rather than by the quantity of lithium available. Because thin foils contain less lithium inventory, they also possess a narrower tolerance window for lithium consumption. As a result, relatively minor differences in surface cleanliness, lithium purity, or microstructural uniformity can disproportionately affect electrochemical behavior, amplifying foil-to-foil variability. Conversely, thicker foils remain buffered against these perturbations because the available lithium is no longer the limiting factor. As shown in Fig. 5e, improvements in the stripping overpotential that correlated with the surface descriptors developed above (including lightness, wettability, metallic lithium purity) have a more pronounced impact on the cycle life of ultrathin foils than on thicker ones. These trends demonstrate that high-quality ultrathin foils have potential to simultaneously deliver high energy density and robust cycling when their initial lithium inventory and surface chemistry are carefully controlled.

Grain Size and Orientation Differences in Lithium Foils

Having established the influence of surface chemistry and lithium inventory on electrochemical behavior, we next examined how bulk microstructure contributes to performance variability. The microstructure of lithium metal is highly sensitive to its manufacturing history, as processes such as casting, rolling, and annealing impose distinct thermal and mechanical pathways that govern grain growth, recovery, and recrystallization.[20, 31, 32, 45, 46] To isolate the effect of microstructure on electrochemical cycling, we compared Foil-5 and foil-6 from the same vendor with comparable nominal thickness and lightness values (Figs. 6a and 6b). EBSD analyses reveal pronounced differences in grain morphology between the two samples. Foil-5 exhibits small grains with elongated, deformation-inherited structures, whereas foil-6 contains much larger equiaxed grains characteristic of more complete recrystallization. Their crystallographic textures also differ substantially, where the small-grained foil-5 shows a preferred (211) orientation, while the large-grained foil-6 exhibits a dominant (110) orientation (Figs. 6c and 6d). Grain-size histograms highlight these contrasts quantitatively: the small-grained foil displays an average equivalent radius of 8.0 μm with a maximum of 13 μm, whereas the large-grained foil averages 41.5 μm and contains grains up to 67 μm (Figs. 6e and 6f). Correspondingly, the large-grained foil delivers higher Coulombic efficiency and significantly slower capacity decay in Li||NMC622 cells, outperforming its fine-grained counterpart under both C/5–D/2 and C/2–D/2 cycling conditions (Figs. 6g and 6h).

The performance difference associated with microstructure arise from several mechanistic factors. First, large grain size reducing grain-boundary density lowers the number of preferential lithium dissolution sites, which otherwise concentrate current and initiate local interfacial instability.[45, 47] PFIB-SEM cross-sections confirm that lithium stripping frequently begins at grain boundaries (**Figures S13 and S14**), supporting their role as electrochemically vulnerable regions. Second, grain boundaries act as high-energy nucleation sites during deposition.[45] During charging, the small-grained foil exhibits a higher nucleation density and more porous lithium growth at boundary regions (**Figure S15**). This porous morphology accelerates active lithium consumption and increases dead-lithium formation, ultimately shortening cycle life. Foils with larger grains suppress both preferential stripping and excessive nucleation, yielding smoother lithium flux and more durable interfaces. The mechanistic trends described here are strongly supported by the present EBSD dataset, which spans a relatively large cross-sectional area (~ 560 μm) and captures clear contrasts between the two samples.

Beyond grain boundary effects, the distinct crystallographic textures of the two foils may also contribute to their performance difference. Recent work has demonstrated that different lithium facets exhibit markedly different self-diffusion barriers.[29, 48] The (110) facet presents the lowest barrier, while (100) and (211) facets show progressively higher values, with lower barriers associated with more uniform deposition morphology and suppressed dendrite formation.[48] In this context, the dominant (100) texture of foil-6 suggests more favorable surface diffusion kinetics compared with the (211) texture of foil-5, which may partially account for the smoother lithium flux and superior cycling stability observed for foil-6. Nevertheless, expanding the dataset to additional foils with diverse microstructures would further strengthen statistical robustness and refine the structure–property correlations observed here, which we regard as an important direction for future work. These findings demonstrate that crystallographic structure is one of the factors of lithium metal anode performance. Manufacturing routes that encourage larger grain sizes, controlled recrystallization, and favorable crystallographic texture can markedly improve cycling stability. Microstructural engineering thus represents a key strategy for producing high-quality lithium metal foils suitable for high-energy battery systems.

While the above results establish a framework for evaluating lithium foil quality under practical conditions, an important question is how such variability can be mitigated or controlled in real-world applications. The descriptors established in this work also point toward actionable strategies for improving foil quality. Recent studies have demonstrated that surface passivation state and crystallographic texture, two key descriptors in our framework, can be actively tuned through post-manufacturing treatments including chemical surface cleaning,[15, 18] mechanically surface polishing,[14] electrochemical polishing,[17] selective etching,[49] controlled recrystallization,[48] and pre-cycling.[50] The screening framework introduced here provides a quantitative baseline against which the efficacy of such treatments can be evaluated. Beyond surface treatment, the temporal evolution of foil quality under varying storage and transportation conditions remains an important open question. The foils in this study represent their as-received state, and a systematic investigation of how calendar aging, humidity, and inert atmosphere quality affect these descriptors would provide crucial guidance for packaging standards and shelf-life specifications across the supply chain.

Conclusion

This study establishes a unified framework linking the initial properties of commercial lithium foils to their electrochemical behavior in lithium metal batteries. By integrating geometric, chemical, optical, and

microstructural analyses across 17 foils, we show that active lithium inventory, surface passivation, and grain structure collectively govern stripping uniformity, interphase growth, and full-cell lifetime. Within this framework, lower metallic lithium purity and lower lightness generally indicate more heterogeneous oxidation layers and higher interfacial resistance, whereas deliberately engineered and chemically uniform coatings protect the lithium surface, maintain low interfacial resistance. Large, well-oriented grains further enhance transport uniformity and interfacial stability, highlighting microstructure as a critical performance driver in commercial lithium foils. Ultrathin foils, which are most attractive for high-energy designs with aggressive N/P ratios, are especially sensitive to these descriptors because of their limited lithium reservoir and narrower tolerance window for lithium consumption. High-quality ultrathin foils defined by favorable values of the proposed descriptors therefore have potential to simultaneously deliver high energy density and robust cycling when lithium inventory and surface chemistry are carefully controlled. The framework introduced here provides practical criteria for qualifying commercial lithium foils and guiding manufacturing, packaging, and coating strategies, and it enables more consistent and predictable implementation of high-energy lithium metal batteries in realistic applications.

Experimental Methods

Materials

1,2,2,2-Tetrafluoroethyl trifluoromethyl ether (TTE, anhydrous, purity ≥ 99%) was obtained from Synquest Laboratories (USA). Battery-grade lithium bis(fluorosulfonyl)imide (LiFSI, purity ≥ 99.95%), 1,2-Dimethoxyethane (DME, purity ≥ 99.0%, inhibitor-free), tetrahydrofuran (THF, anhydrous, purity ≥ 99.9%, inhibitor-free), biphenyl (purity ≥ 99.0%), H_2SO_4 (95 wt% in H_2O) and H_2O_2 (30% in H_2O) were purchased from Sigma-Aldrich (USA). Before use, all solvents were dried over molecular sieves to remove residual moisture. NCM622 cathodes (22.28 mg/cm^2, 4.01 mAh/cm^2 based on 180 mAh/g) were kindly provided by Pacific Northwest National Laboratory. Lithium foils from nine different vendors were received in their respective packaging. Upon receipt, the samples were transferred into and stored inside an argon- filled glovebox with < 0.2 ppm O_2 and < 0.1 ppm H_2O.

Characterization

Surface color and electrolyte contact angle. Surface color analysis was performed using a portable color analyzer (CTI, China) equipped with a D65 light source in the International Commission on Illumination (CIE) Lab color space. The colorimeter was calibrated with pure white and black before measurements. Contact angle measurements were conducted using a customized contact angle meter inside an argon-filled glovebox. Lithium foils were cut to 1 cm × 1 cm squares and backlit. A 5 uL droplet of electrolyte (1.54 M LiFSI in DME/TTE, 22/78 v/v%) was placed on the lithium surface, and the angle between the foil surface and the droplet curvature was captured using a digital camera. All procedures were performed in an argon-filled glove box (< 0.2 ppm O_2, < 0.1 ppm H_2O).

Scanning electron microscopy. Lithium foils obtained from different vendors were imaged from their pristine state without washing. Li anodes after cycling were retrieved from disassembled coin cells and rinsed with DME to remove residual electrolyte and salt before imaging. Cross-sectional imaging was performed using a Helios Hydra 5 PFIB–SEM equipped with a CleanConnect inert-gas transfer system (Thermo Fisher Scientific, USA) at room temperature. A xenon ion beam operated at 30 kV and 15 nA was used for coarse milling, followed by final

polishing at 1 nA. Cross-sectional SEM images were acquired using a secondary electron detector (SED) at 5 kV and 0.1 nA. Statistical error ranges were obtained from three measurements across a 30 μm-wide cross-section.

Surface imaging with energy-dispersive X-ray spectroscopy (SEM–EDX) and electron backscatter diffraction (EBSD) was conducted on a Helios 5CX FIB–SEM (Thermo Fisher Scientific, USA) under cryogenic conditions. Samples were transferred to the SEM chamber under inert-gas protection and maintained at ≤–170°C. The sample stage was cooled to − 180°C using liquid N_2 to create a cryogenic environment and minimize beam-induced damage. SEM–EDX mapping was carried out at 20 kV and 1.6 nA. EBSD patterns and maps were collected using an Oxford Instrument Symmetry EBSD camera at 7 kV and 6.4 nA.

Lithium purity tests. Purity of lithium foils in their pristine state were characterized by previously established methods.[51, 52] Titration gas chromatography (TGC) was performed to quantify the amount of metallic Li^0 and inductively coupled plasma mass spectrometry (ICP-MS, Thermo Fisher iCAP Q, USA) was used to determine the total Li amount (Li^0 + Li^+). TGC was conducted on the Shimadzu GC-2010 Plus Tracera equipped with a barrier ionization discharge (BID) detector. Samples from each lithium foil were transferred into glass flasks and sealed with septum inside an argon-filled glovebox. After removal from the glovebox, deionized water was injected into each flask to fully react with Li. A gas-tight syringe was then used to transfer the resulting gas into the gas chromatograph. The amount of metallic Li^0 was calculated based on the quantified H_2 generated, using a pre-established standard calibration curve.

To determine the total lithium content and metal impurities, the solution with Li^0 digested from the TGC test was further digested with H_2SO_4 (95 wt% in H_2O) and H_2O_2 (30% in H_2O) solution at 60°C for 24 hours. The amount of total Li along with Na, Fe, and Mg impurities were then quantified by ICP-MS with pre-established standard calibration curves.

X-ray photoelectron spectroscopy and Time-of-Flight Secondary Ion Mass Spectrometry. X-ray photoelectron spectroscopy (XPS) was performed on a NEXSA G2 system (Thermo Fisher Scientific, USA) using Al K-Alpha X-ray source. Survey scans were acquired with a step size of 1.0 eV, followed by fine scans with 0.1 eV resolution. Depth profiles were built by monatomic Ar^+ source etching under 4 keV voltage. Spectra were analyzed using CasaXPS software to identify and quantify different chemical species. Fitting parameters used to identify different compounds on metallic lithium surface based on literature and experimental evidence are listed in Tables S3-S5.[26, 53] For foils with low or negligible amounts of Li_2CO_3, a single peak was used in the O 1s region to fit both LiOH and Li_2CO_3 for the close binding energy of the two components. Time-of-Flight Secondary Ion Mass Spectrometry (ToF-SIMS) was conducted using ION TOF M6 using Ar clusters for milling with 0.33 nm/sec etching rate. Both cycled electrodes for XPS and ToF-SIMS tests were transferred to an air-tight holder assembled in an Ar-filled glovebox to avoid air exposure.

Surface Profilometry. Surface topography of all 17 lithium foils was characterized using a 3D laser scanning confocal microscope (Keyence VK-X1000) with a 20× objective lens. To prevent surface oxidation during measurement, samples were mounted in a custom-built airtight chamber filled with argon and equipped with a glass optical window to allow optical access. Three non-overlapping surface maps were acquired per foil, and the mean surface roughness was calculated for each foil and averaged across the three maps to obtain a representative value.

Electrochemical tests. The electrolyte was prepared by dissolving LiFSI in a DME/TTE mixture (22/78 v/v%) at a concentration of 1.54 M. Li||Cu CR2032 coin cells were assembled to evaluate the stripping behavior of the lithium foils. A 10 μm-thick copper disc was used as the working electrode, while a lithium metal foil served as both the reference and counter electrode. A 20 μm-thick polyethylene (PE) separator was employed, and each cell was filled with 75 μL of electrolyte. Lithium was stripped at a current density of 1 mA/cm^2 until − 1 V was reached.

The full cell cycling performance of the lithium foils was evaluated in CR2032 coin cells with NMC622 cathode (22.28 mg/cm^2, 4.01 mAh/cm^2 based on 180 mAh/g). A 20 μm-thick polyethylene (PE) separator was employed. Each cell contained 18 g/Ah of electrolyte. Cells were charged with a constant current at 25°C in an environmental test chamber (Neware, China) to 4.4V and discharged to 2.8 V. The cells were cycled at C/10 charge rate and D/10 discharge rate (1C = 4 mA/cm^2) for two formation cycles, followed by continuous cycling at different rates until 80% capacity retention was reached. Detailed SOP of full cell assembly and testing can be found in the **Supplementary Note**.

Declarations

Conflicts of Interest

The authors declare no conflicts of interest.

Author Contribution

K. W., S. D., W. B., and Y.S.M. conceived the idea and designed the experiments. K. W. and S. D. carried out the colorimetry testing and data analysis. K. W. performed the contacting angle measurement and data analysis. K. W., S. D., and V. J. performed electrochemical testing and data analysis. K. W., S. D., B. B., and K. H. conducted the PFIB results. K. W. and B. B. obtained the SEM-EDX results. S. D. performed ToF-SIMS and data analysis. W. B. performed TGC and data analysis. K. H. performed profilometry and data analysis. W. B., K. R, and B. B. performed ICP-MS and ICP-OES. B. B. performed EBSD and data analysis. S. W. and M. L. performed the XPS experiment and data analysis. K. W., S. D., K. H., W. B., and Y.S.M. organized the work and helped with the draft of the manuscript. All the authors discussed the results and approved the final version of the manuscript.

Acknowledgement

This work was funded by Elevated Materials and The Energy Transition Network. PFIB data were collected at the Center for Nanoscale Materials, a U.S. Department of Energy Office of Science User Facility, supported by the U.S. Department of Energy, Office of Basic Energy Sciences, under Contract No. DE-AC02-06CH11357. EBSD experiments were conducted at the Core Center of Excellence in Nano Imaging at the University of Southern California. The authors thank Pacific Northwest National Laboratory and the Cell Analysis, Modeling, and Prototyping (CAMP) Facility at Argonne National Laboratory for providing the cathode sheets. The authors also acknowledge the use of facilities at the Research Resources Center at the University of Illinois Chicago and the Northwestern University Atomic and Nanoscale Characterization Experimental Center.

Data Availability

Data utilized in this work are available from the corresponding author upon reasonable request.

References

1. Yang, X.; Zhang, H.; Liu, Q.; Jiang, G. The Li-ion battery industry and its challenges. *Nature Reviews Chemistry* 2025, 1–2.
2. Zhao, H.; Zuo, H.; Wang, J.; Jiao, S. Practical application of graphite in lithium-ion batteries: Modification, composite, and sustainable recycling. *Journal of Energy Storage* 2024, *98*, 113125.
3. Yi, X.; Qi, G.; Liu, X.; Depcik, C.; Liu, L. Challenges and strategies toward anode materials with different lithium storage mechanisms for rechargeable lithium batteries. *Journal of Energy Storage* 2024, *95*, 112480.
4. Orangi, S.; Manjong, N.; Clos, D. P.; Usai, L.; Burheim, O. S.; Strømman, A. H. Historical and prospective lithium-ion battery cost trajectories from a bottom-up production modeling perspective. *Journal of Energy Storage* 2024, *76*, 109800.
5. Wang, J.; Ge, B.; Li, H.; Yang, M.; Wang, J.; Liu, D.; Fernandez, C.; Chen, X.; Peng, Q. Challenges and progresses of lithium-metal batteries. *Chemical Engineering Journal* 2021, *420*, 129739.
6. Lin, D.; Liu, Y.; Cui, Y. Reviving the lithium metal anode for high-energy batteries. *Nature nanotechnology* 2017, *12* (3), 194–206.
7. Acebedo, B.; Morant-Miñana, M. C.; Gonzalo, E.; Ruiz de Larramendi, I.; Villaverde, A.; Rikarte, J.; Fallarino, L. Current status and future perspective on lithium metal anode production methods. *Advanced Energy Materials* 2023, *13* (13), 2203744.
8. Huang, H.; Hu, Y.; Hou, Y.; Wang, X.; Dong, Q.; Zhao, Z.; Ji, M.; Zhang, W.; Li, J.; Xie, J. Delocalized electrolyte design enables 600 Wh kg – 1 lithium metal pouch cells. *Nature* 2025, 1–8.
9. He, M.; Hector Jr, L. G.; Dai, F.; Xu, F.; Kolluri, S.; Hardin, N.; Cai, M. Industry needs for practical lithium-metal battery designs in electric vehicles. *Nature Energy* 2024, *9* (10), 1199–1205.
10. Meng, Y. S.; Srinivasan, V.; Xu, K. Designing better electrolytes. *Science* 2022, *378* (6624), eabq3750.
11. Zhang, H.; Zeng, Z.; Cheng, S.; Xie, J. Recent progress and perspective on lithium metal battery with nickel-rich layered oxide cathode. *eScience* 2024, *4* (6), 100265.
12. Liu, J.; Bao, Z.; Cui, Y.; Dufek, E. J.; Goodenough, J. B.; Khalifah, P.; Li, Q.; Liaw, B. Y.; Liu, P.; Manthiram, A. Pathways for practical high-energy long-cycling lithium metal batteries. *Nature Energy* 2019, *4* (3), 180–186.
13. Hatzell, K.; Chang, W.; Bao, W.; Cai, M.; Glossmann, T.; Kalnaus, S.; Liaw, B.; Meng, Y. S.; Mohtadi, R.; Wang, Y. Aligning lithium metal battery research and development across academia and industry. *Joule* 2024, *8* (6), 1550–1555.
14. Hu, Y.; Li, Y.; Hou, H.; Chen, Z.; Chen, Y.; Iqbal, N.; Liu, W. Surface-finish induced textured electrodeposition on 20 μm Li-metal anode. *Energy Storage Materials* 2025, *76*, 104160.
15. Hu, M.; Tong, Z.; Cui, C.; Zhai, T.; Li, H. Facile, atom-economic, chemical thinning strategy for ultrathin lithium foils. *Nano Letters* 2022, *22* (7), 3047–3053.
16. Baek, M.; Kim, J.; Jeong, K.; Yang, S.; Kim, H.; Lee, J.; Kim, M.; Kim, K. J.; Choi, J. W. Naked metallic skin for homo-epitaxial deposition in lithium metal batteries. *Nature Communications* 2023, *14* (1), 1296.

17. Shi, K.; Dutta, A.; Hao, Y.; Zhu, M.; He, L.; Pan, Y.; Xin, X.; Huang, L. F.; Yao, X.; Wu, J. Electrochemical polishing: an effective strategy for eliminating Li dendrites. *Advanced Functional Materials* 2022, *32* (33), 2203652.
18. Tang, W.; Yin, X.; Chen, Z.; Fu, W.; Loh, K. P.; Zheng, G. W. Chemically polished lithium metal anode for high energy lithium metal batteries. *Energy Storage Materials* 2018, *14*, 289–296.
19. Mashtalir, O.; Nguyen, M.; Bodoin, E.; Swonger, L.; O'Brien, S. P. High-purity lithium metal films from aqueous mineral solutions. *ACS omega* 2018, *3* (1), 181–187.
20. Zhang, H.; Chen, D.; Lai, J.; Shi, F. Understanding the Surface Passivation and Crystallographic Orientation Effects of Commercial Lithium Metal Anodes on Battery Performance. *ACS Applied Energy Materials* 2025.
21. Becker, J.; Weintraut, T.; Benz, S. L.; Fuchs, T.; Lerch, C.; Becker, P.; Eckhardt, J. K.; Henß, A.; Richter, F. H.; Janek, J. Purity of lithium metal electrode and its impact on lithium stripping in solid-state batteries. *Nature Communications* 2025, *16* (1), 5395.
22. Otto, S.-K.; Fuchs, T.; Moryson, Y.; Lerch, C.; Mogwitz, B.; Sann, J.; Janek, J. r.; Henss, A. Storage of lithium metal: the role of the native passivation layer for the anode interface resistance in solid state batteries. *ACS Applied Energy Materials* 2021, *4* (11), 12798–12807.
23. Koch, S. L.; Morgan, B. J.; Passerini, S.; Teobaldi, G. Density functional theory screening of gas-treatment strategies for stabilization of high energy-density lithium metal anodes. *Journal of Power Sources* 2015, *296*, 150–161.
24. Etxebarria, A.; Koch, S. L.; Bondarchuk, O.; Passerini, S.; Teobaldi, G.; Muñoz-Márquez, M. Á. Work function evolution in Li anode processing. *Advanced Energy Materials* 2020, *10* (24), 2000520.
25. Ho, A. S.; Westover, A. S.; Browning, K.; Maslyn, J. A.; Parkinson, D. Y.; Sahore, R.; Dudney, N.; Balsara, N. P. Comparing the purity of rolled versus evaporated lithium metal films using X-ray microtomography. *ACS Energy Letters* 2022, *7* (3), 1120–1124.
26. Etxebarria, A.; Yun, D.-J.; Blum, M.; Ye, Y.; Sun, M.; Lee, K.-J.; Su, H.; Muñoz-Márquez, M. A. n.; Ross, P. N.; Crumlin, E. J. Revealing in situ Li metal anode surface evolution upon exposure to CO2 using Ambient Pressure X-ray Photoelectron Spectroscopy. *ACS Appl. Mater. Interfaces* 2020, *12* (23), 26607–26613.
27. Li, Y.; Liu, Q.; Wu, S.; Geng, L.; Popovic, J.; Li, Y.; Chen, Z.; Wang, H.; Wang, Y.; Dai, T. Unraveling the reaction mystery of Li and Na with dry air. *Journal of the American Chemical Society* 2023, *145* (19), 10576–10583.
28. Li, Y.; Li, Y.; Sun, Y.; Butz, B.; Yan, K.; Koh, A. L.; Zhao, J.; Pei, A.; Cui, Y. Revealing nanoscale passivation and corrosion mechanisms of reactive battery materials in gas environments. *Nano Lett.* 2017, *17* (8), 5171–5178.
29. Tan, J.; Ma, L.; Yi, P.; Wang, Y.; Li, Z.; Fang, Z.; Li, X.; He, S.; Wang, X.; Ye, M. Scalable Customization of Crystallographic Plane Controllable Lithium Metal Anodes for Ultralong-Lasting Lithium Metal Batteries. *Advanced Materials* 2024, *36* (30), 2403570.
30. Hu, X.; Gao, Y.; Zhang, B.; Shi, L.; Li, Q. Superior cycle performance of Li metal electrode with {110} surface texturing. *EcoMat* 2022, *4* (6), e12264.
31. Wu, Z.; Wang, C.; Hui, Z.; Liu, H.; Wang, S.; Yu, S.; Xing, X.; Holoubek, J.; Miao, Q.; Xin, H. L. Growing single-crystalline seeds on lithiophobic substrates to enable fast-charging lithium-metal batteries. *Nature Energy* 2023, *8* (4), 340–350.
32. Zhao, Q.; Deng, Y.; Utomo, N. W.; Zheng, J.; Biswal, P.; Yin, J.; Archer, L. A. On the crystallography and reversibility of lithium electrodeposits at ultrahigh capacity. *Nature Communications* 2021, *12* (1), 6034.

33. Shi, F.; Pei, A.; Vailionis, A.; Xie, J.; Liu, B.; Zhao, J.; Gong, Y.; Cui, Y. Strong texturing of lithium metal in batteries. *Proceedings of the National Academy of Sciences* 2017, *114* (46), 12138–12143.
34. Guo, R.; Gallant, B. M. Li2O solid electrolyte interphase: probing transport properties at the chemical potential of lithium. *Chemistry of Materials* 2020, *32* (13), 5525–5533.
35. Zheng, S.; Geng, H.; Eliseeva, S. N.; Wang, B. Air-exposed lithium metal as a highly stable anode for low-temperature energy storage applications. *Energy Materials* 2022, *2* (6), N/A-N/A.
36. Seok, J.; Gannett, C. N.; Yu, S.-H.; Abruna, H. D. Understanding the impacts of Li stripping overpotentials at the counter electrode by three-electrode coin cell measurements. *Analytical chemistry* 2021, *93* (46), 15459–15467.
37. Mohammadi, A.; Monconduit, L.; Stievano, L.; Younesi, R. Measuring the nucleation overpotential in lithium metal batteries: never forget the counter electrode! *Journal of The Electrochemical Society* 2022, *169* (7), 070509.
38. Ren, X.; Zou, L.; Cao, X.; Engelhard, M. H.; Liu, W.; Burton, S. D.; Lee, H.; Niu, C.; Matthews, B. E.; Zhu, Z. Enabling high-voltage lithium-metal batteries under practical conditions. *Joule* 2019, *3* (7), 1662–1676.
39. Li, Y.; Qi, Y. Transferable self-consistent charge density functional tight-binding parameters for Li–metal and Li-ions in inorganic compounds and organic solvents. *The Journal of Physical Chemistry C* 2018, *122* (20), 10755–10764.
40. Kamphaus, E. P.; Angarita-Gomez, S.; Qin, X.; Shao, M.; Engelhard, M.; Mueller, K. T.; Murugesan, V.; Balbuena, P. B. Role of inorganic surface layer on solid electrolyte interphase evolution at Li-metal anodes. *ACS applied materials & interfaces* 2019, *11* (34), 31467–31476.
41. Phillips, J.; Tanski, J. Structure and kinetics of formation and decomposition of corrosion layers formed on lithium compounds exposed to atmospheric gases. *International materials reviews* 2005, *50* (5), 265–286.
42. Wu, W.; Luo, W.; Huang, Y. Less is more: a perspective on thinning lithium metal towards high-energy-density rechargeable lithium batteries. *Chemical Society Reviews* 2023, *52* (8), 2553–2572.
43. Neumann, J.; Hellweg, L.; Bela, M.; Hering, T.; Stan, M.; Winter, M.; Nowak, S.; Börner, M. The role of lithium metal electrode thickness on cell safety. *Cell Reports Physical Science* 2025, *6* (1).
44. Niu, C.; Liu, D.; Lochala, J. A.; Anderson, C. S.; Cao, X.; Gross, M. E.; Xu, W.; Zhang, J.-G.; Whittingham, M. S.; Xiao, J. Balancing interfacial reactions to achieve long cycle life in high-energy lithium metal batteries. *Nature Energy* 2021, *6* (7), 723–732.
45. Sun, X.; Feng, Y.; Yu, J.; Lu, Y.; Xu, S.; Jiang, Y.; Li, H.; Yan, Z.; Zhang, K.; Chen, J. Eliminating intercrystalline side effects for stable lithium metal batteries. *Proceedings of the National Academy of Sciences* 2025, *122* (45), e2507789122.
46. Zhang, M.; Tantratian, K.; Ham, S.-Y.; Wang, Z.; Chouchane, M.; Shimizu, R.; Bai, S.; Yang, H.; Liu, Z.; Li, L. Grain selection growth of soft metal in electrochemical processes. *Joule* 2025, *9* (4).
47. Shi, F.; Pei, A.; Boyle, D. T.; Xie, J.; Yu, X.; Zhang, X.; Cui, Y. Lithium metal stripping beneath the solid electrolyte interphase. *Proceedings of the National Academy of Sciences* 2018, *115* (34), 8529–8534.
48. Chen, H.; Zhao, Y.; Zhang, X.; Li, R.; Wang, A.; Zhang, H.; Liu, J.; Wen, B.; Zhang, L.; Hua, Q. Synthesis of monocrystalline lithium for high-critical-current-density solid-state batteries. *Nature Synthesis* 2025, *4* (5), 552–561.

49. Song, W.; Chen, M.; Ban, D.; Miao, X.; Huang, J. Chemically etched lithium metal anode with a quasi-single-crystalline (110) surface. *Watt* 2026, *1* (1), 6.
50. Hou, G.; Ma, X.; Sun, Q.; Ai, Q.; Xu, X.; Chen, L.; Li, D.; Chen, J.; Zhong, H.; Li, Y. Lithium dendrite suppression and enhanced interfacial compatibility enabled by an ex situ SEI on Li anode for LAGP-based all-solid-state batteries. *ACS applied materials & interfaces* 2018, *10* (22), 18610–18618.
51. Fang, C.; Li, J.; Zhang, M.; Zhang, Y.; Yang, F.; Lee, J. Z.; Lee, M.-H.; Alvarado, J.; Schroeder, M. A.; Yang, Y. Quantifying inactive lithium in lithium metal batteries. *Nature* 2019, *572* (7770), 511–515.
52. Deng, W.; Yin, X.; Bao, W.; Zhou, X.; Hu, Z.; He, B.; Qiu, B.; Meng, Y. S.; Liu, Z. Quantification of reversible and irreversible lithium in practical lithium-metal batteries. *Nature Energy* 2022, *7* (11), 1031–1041.
53. Wood, K. N.; Teeter, G. XPS on Li-battery-related compounds: analysis of inorganic SEI phases and a methodology for charge correction. *ACS Applied Energy Materials* 2018, *1* (9), 4493–4504.

Figures

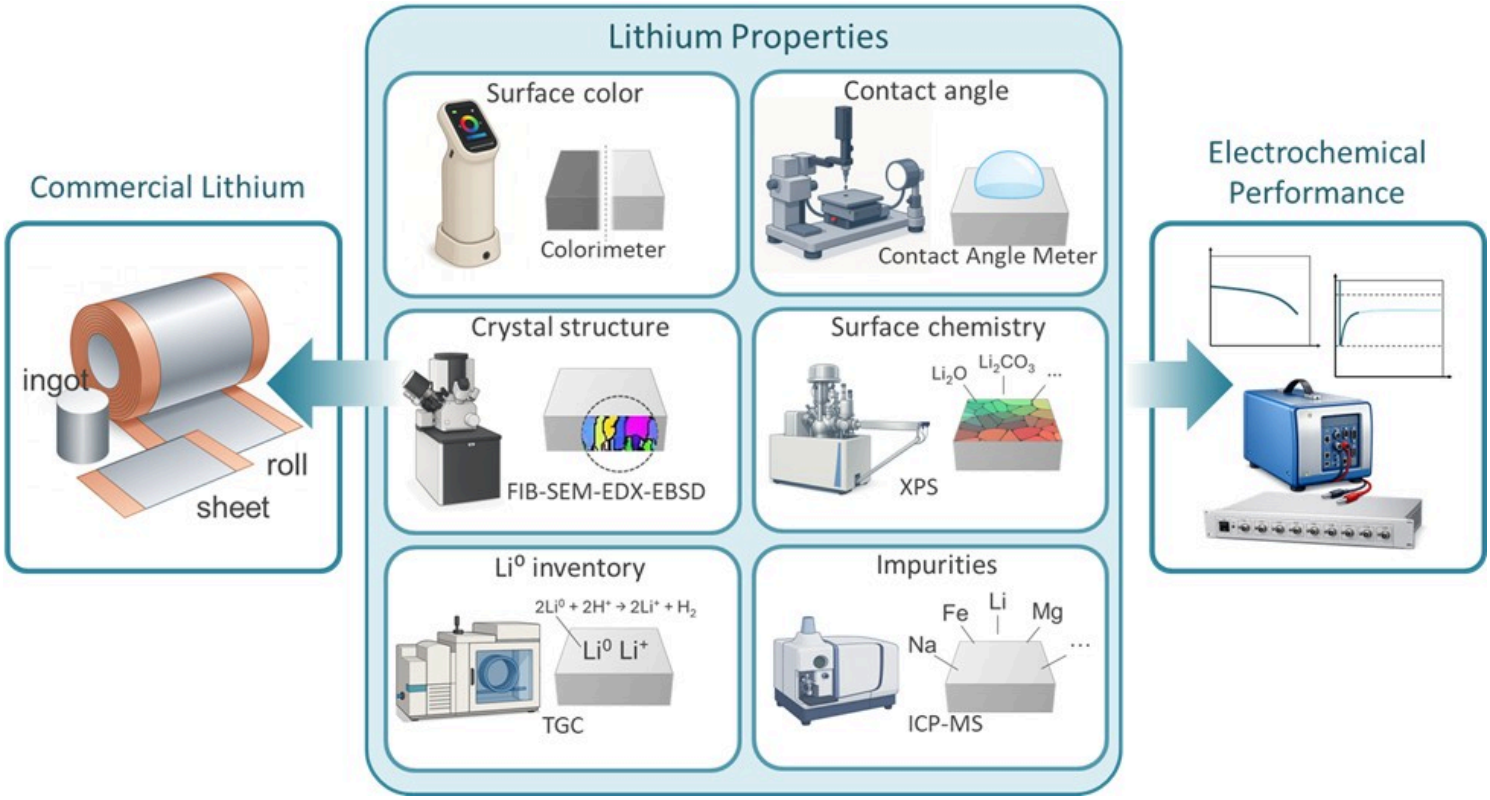

Figure 1

Characterization workflow using integrated metrology tools for comprehensive analysis of lithium metal foil prior to is application in LMBs.

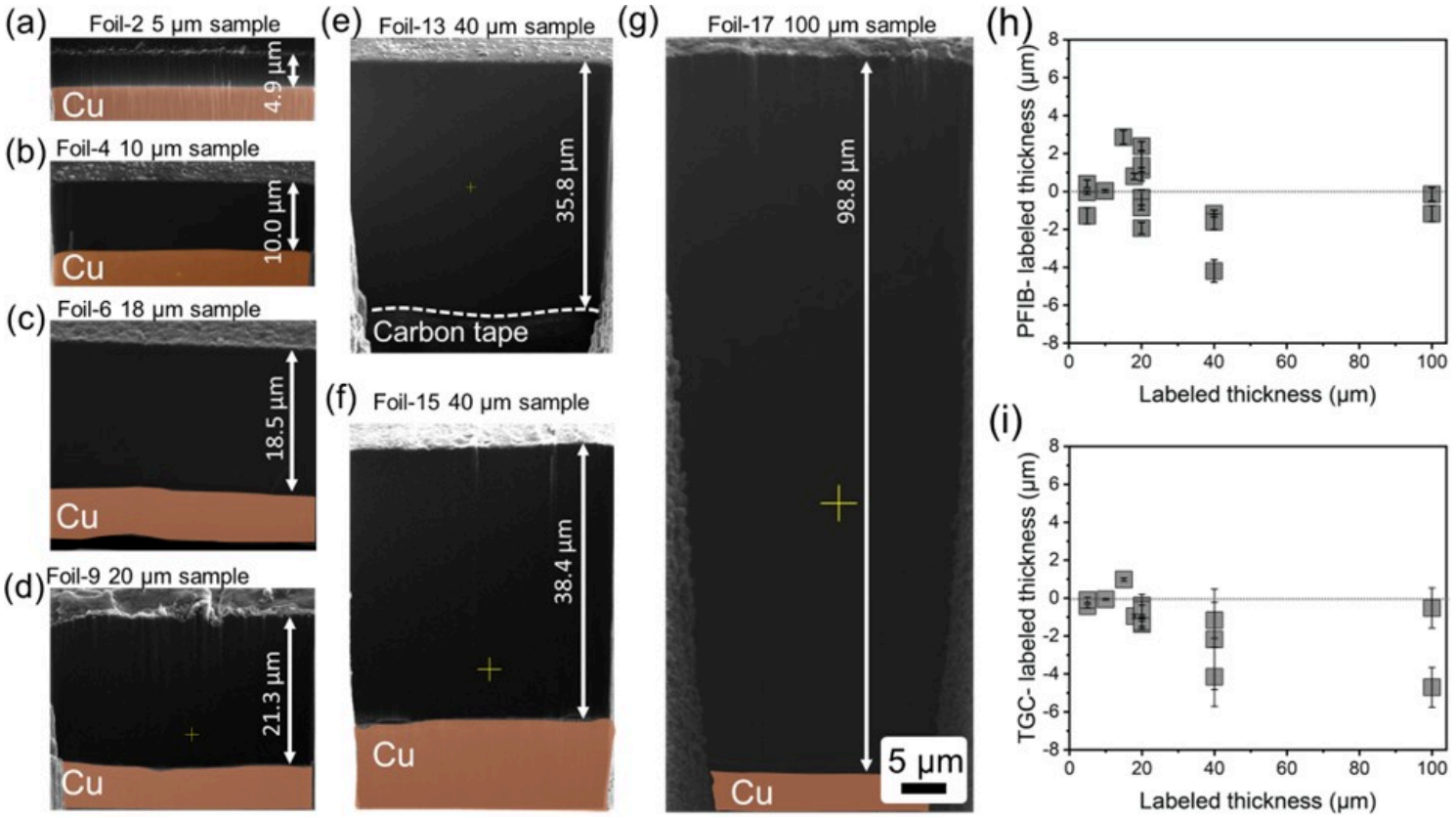

Figure 2

Quantifying active metallic lithium content. (a-g) PFIB-SEM cross-section morphology lithium foils ranging from 5 μm to 100 μm. (h) Lithium thickness measured from the PFIB-SEM cross-section compared to the labeled thickness. (i) Equivalent metallic lithium thickness measured by TGC compared to labeled thickness.

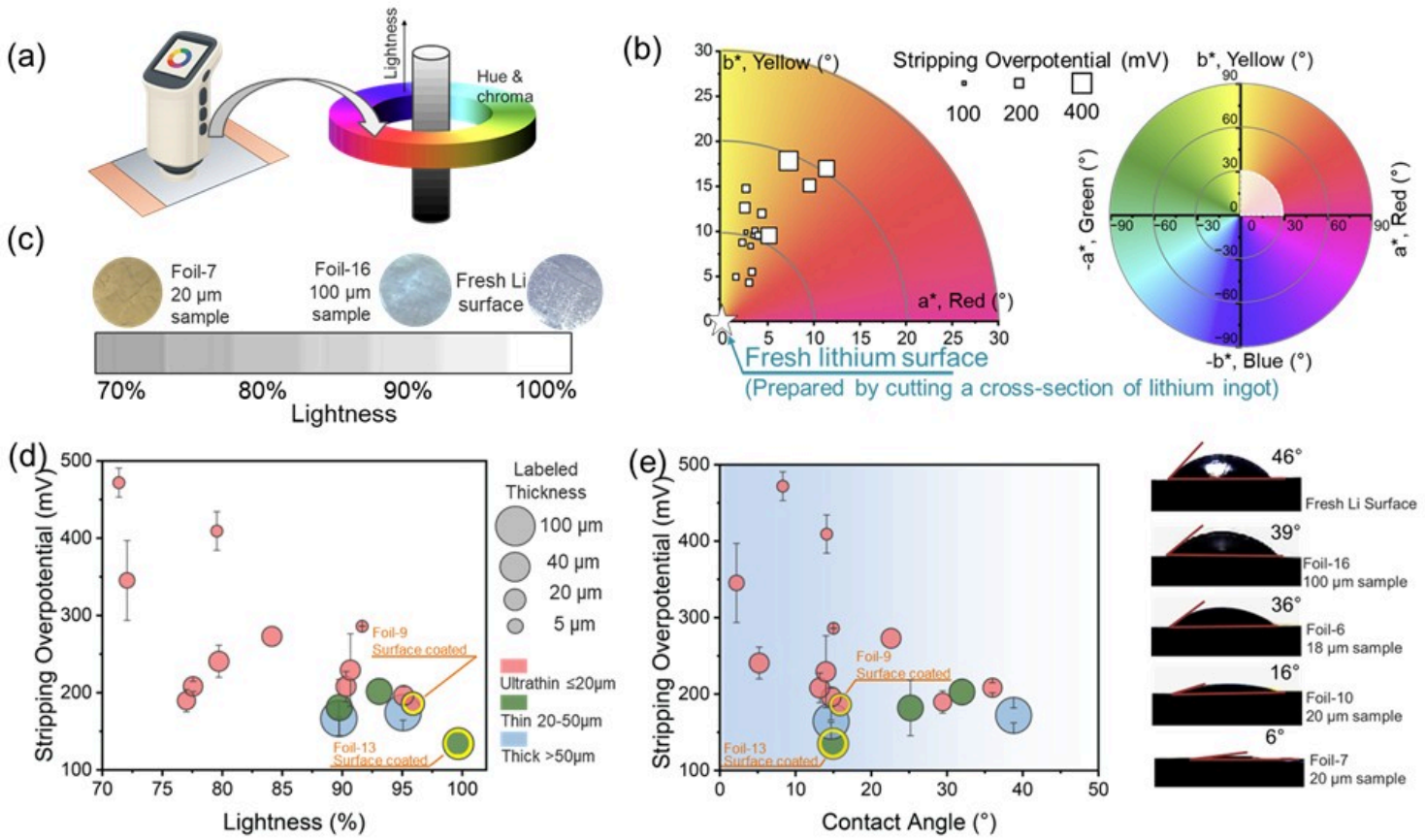

Figure 3

(a) Schematic illustration of color space measurements of lithium metal using a colorimeter. (b) Hue and chroma map of lithium metal samples. The size of the sample spot represents the stripping overpotential of the sample in a Li || Cu cell. The full color map is shown on the right side, where the focused sector is marked in white. (c) Photographic comparison of selected lithium foils arranged by surface lightness. (d) Stripping overpotential in a Li || Cu cell as a function of Li foil surface lightness. (e) Surface contact angle of localized high-concentration electrolyte (LHCE, 1.54 M LiFSI in DME:TTE = 22/78 v/v%) on lithium metal foil. Correlation between LHCE contact angle and stripping overpotential in a Li || Cu cell.

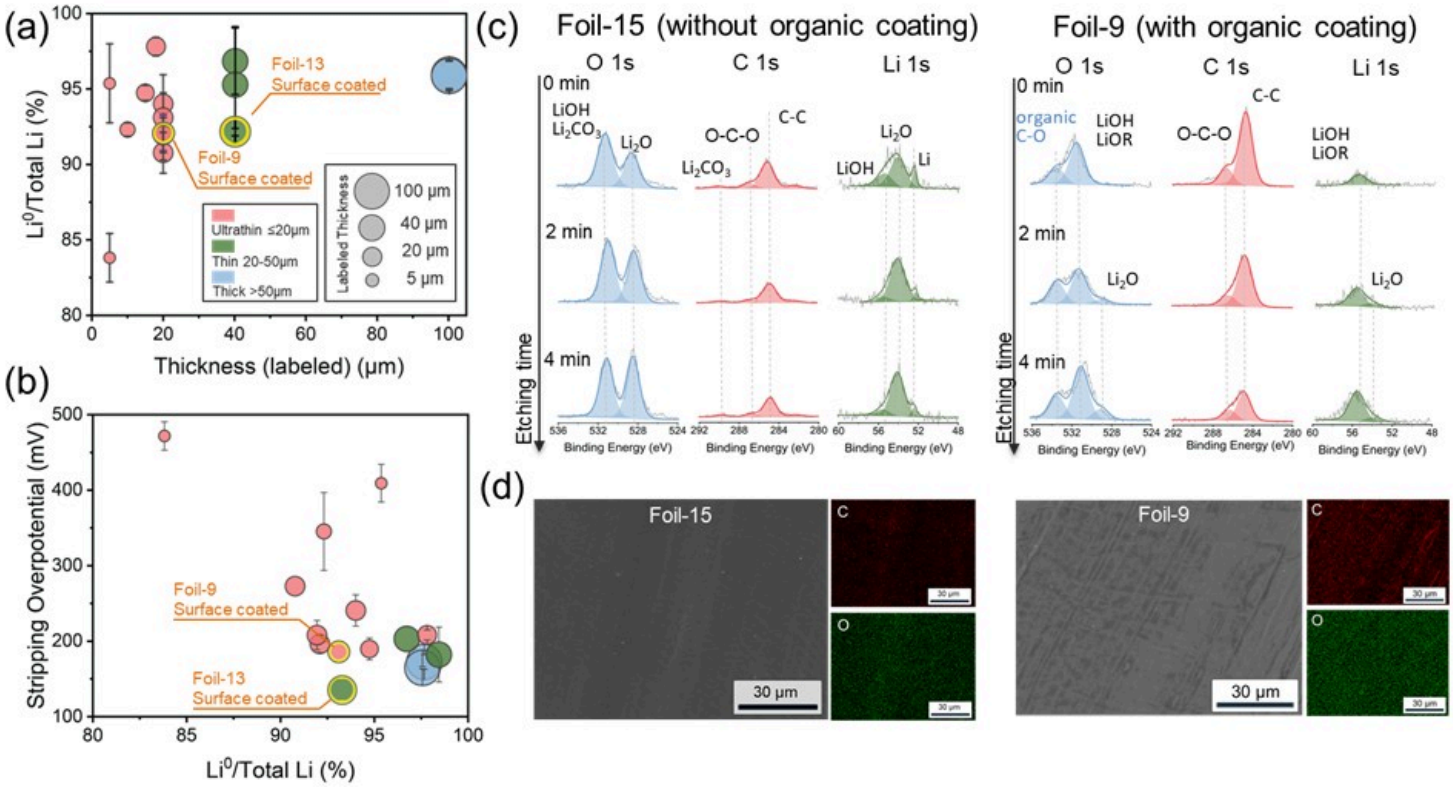

Figure 4

(a) Lithium foil labeled thickness as a function of lithium purity. (b) Lithium purity as a function of stripping overpotential in Li||Cu cells. (c) XPS spectra of Foil-15 40 μm sample and Foil-9 20 μm sample. (d) Surface morphology and elemental mapping via SEM-EDX for Foil-15 40 μm sample and Foil-9 20 μm sample.

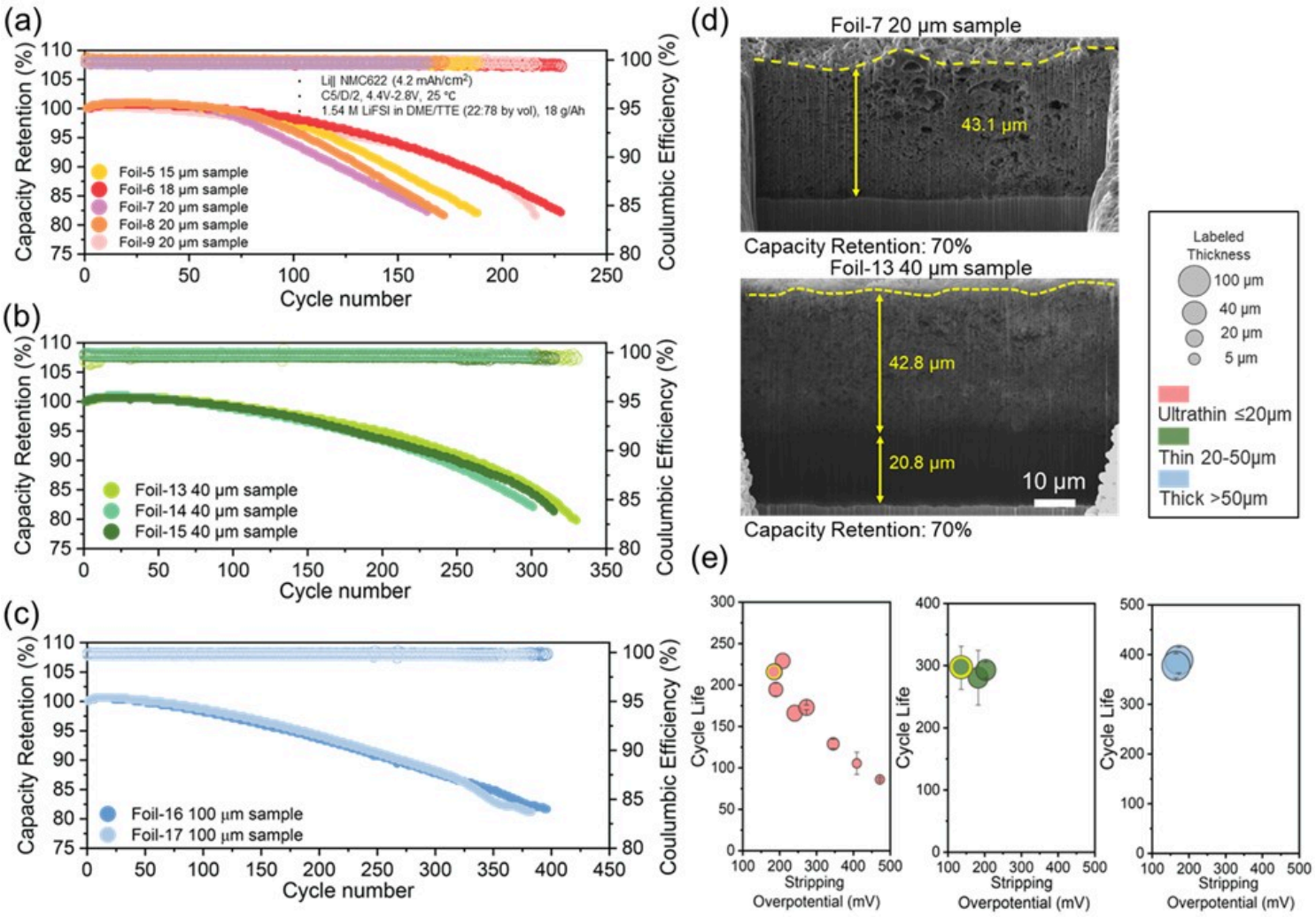

Figure 5

Capacity retention over cycles in Li||NMC622 full cells using (a) ultrathin lithium foils (b) thin lithium foils, and (c) thick lithium foils. (d) PFIB-SEM cross-section images of LMAs after reaching 70% capacity retention with different initial lithium thickness. (e) Cycle life of lithium foils in Li||NMC622 full cells as a function of stripping overpotential in Li||Cu cells.

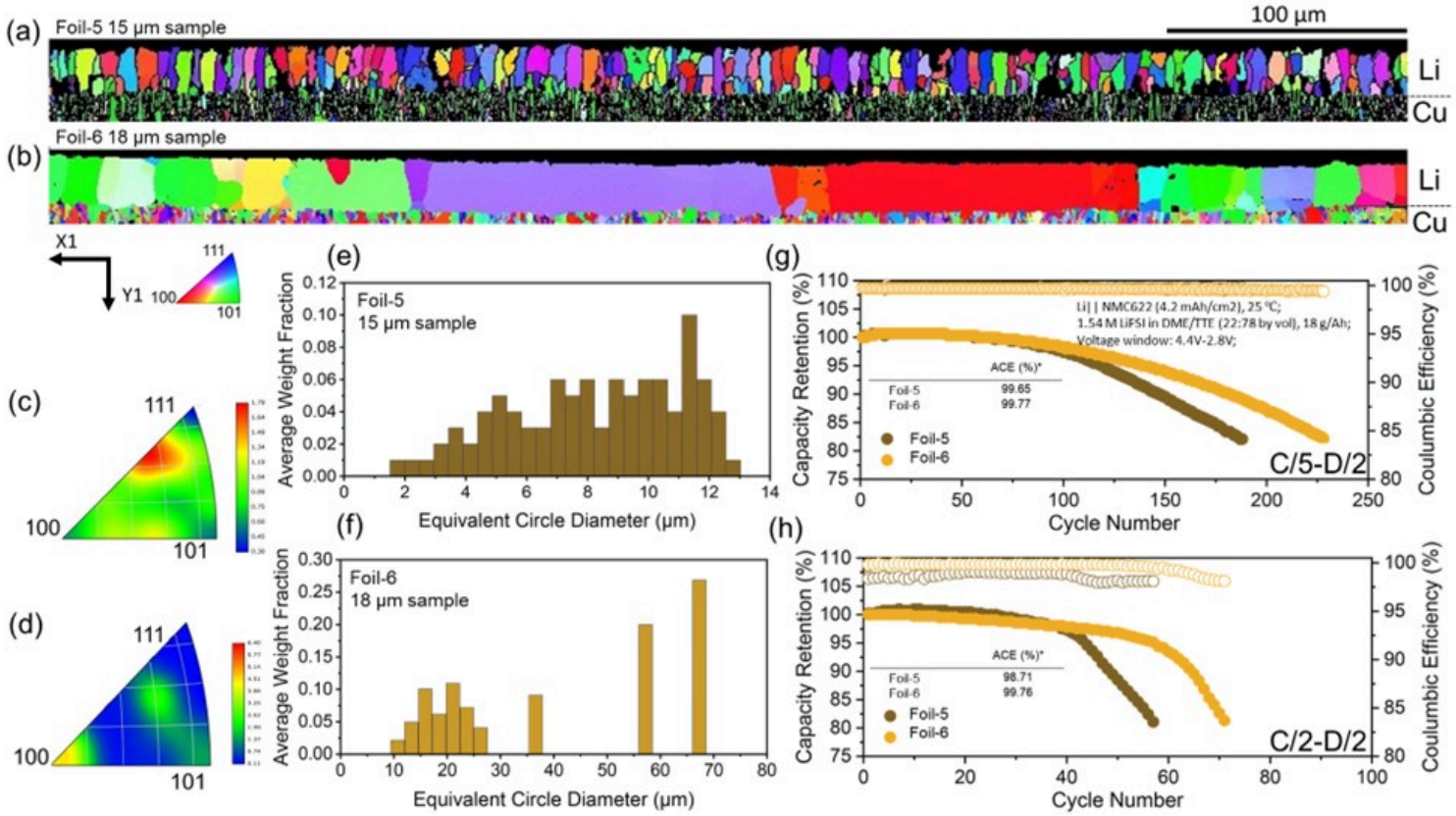

Figure 6

EBSD mapping results along the growth direction, the inverse pole figures, and grain size analysis of (a, c, e) foil-5 15 µm sample and (b, d, f) foil-6 18 µm sample. Cycling performance of Foil-5 15 µm sample and Foil-6 18 µm sample in Li|NMC622 at (g) C/5 charge rate and D/2 discharge rate h) C/2 charge rate and D/2 discharge rate.

Supplementary Files

This is a list of supplementary files associated with this preprint. Click to download.

- IntrinsicVariabilityofLithiumMetalFoilsandItsImpactonRechargeableBatteryPerformanceSICleanVersion.docx